

Echoes of Self-Interacting Dark Matter from Binary Black Hole Mergers

Amitayus Banik,^{1,2,*} Jeong Han Kim,^{1,†} Jun Seung Pi,^{1,‡} and Yuhsin Tsai^{3,§}

¹*Department of Physics, Chungbuk National University, Cheongju, Chungbuk 28644, Korea*

²*Research Institute for Nanoscale Science and Technology,
Chungbuk National University, Cheongju, Chungbuk 28644, Korea*

³*Department of Physics and Astronomy, University of Notre Dame, IN 46556, USA*

Dark matter (DM) environments around black holes (BHs) can influence their mergers through dynamical friction, causing gravitational wave (GW) dephasing during the inspiral phase. While this effect is well studied for collisionless dark matter (CDM), it remains unexplored for self-interacting dark matter (SIDM) due to the typically low DM density in SIDM halo cores. In this work, we show that SIDM models with a massive force mediator can support dense enough DM spikes, significantly affecting BH mergers and producing a distinct GW dephasing. Using N -body simulations, we analyze GW dephasing in binary BH inspirals within CDM and SIDM spikes. By tracking the binary's motion in different SIDM environments, we show that the Laser Interferometer Space Antenna (LISA) can distinguish DM profiles shaped by varying DM interaction strengths, revealing detailed properties of SIDM.

Introduction. Gravitational wave (GW) observations [1–5] have significantly enhanced our understanding of the universe, offering a powerful tool to study previously inaccessible physics [6–10]. By analyzing GW signals with present and forthcoming detectors, such as the Laser Interferometer Space Antenna (LISA) [11–14], we can probe dark sector interactions beyond the Standard Model with remarkable precision. This approach enables the exploration of dark matter (DM) scenarios that evade direct detection via SM interactions, expanding the scope of DM search through purely gravitational effects.

Intermediate-mass black holes (BHs) with masses of $\sim 10^2 - 10^5 M_\odot$ are believed to form in the centers of dwarf galaxies and globular clusters [15], with a single galaxy potentially containing multiple such BHs [16–19]. In particular, intermediate-mass BHs can host dense DM regions known as mini-spikes. Such structures typically form via the adiabatic growth of small black hole seeds situated at the centers of DM halo [17, 20, 21]. While the orbital motion of heavier BHs can disrupt their host DM spikes, this effect is milder for intermediate-mass BHs [22–25]. As a result, the surrounding DM structures may retain enough density to resist tidal disruptions, making it plausible that mini-spikes around intermediate-mass BHs have survived to the present day.

The persistence of these DM mini-spikes has significant implications for GW observations. Dynamical friction between DM mini-spikes and intermediate-mass BHs can perturb the orbits in binary systems, significantly affecting their emitted GWs. The cumulative effects of these interactions result in phase shifts in the gravitational waveforms, leading to observable deviations from the expected predictions without DM. This phenomenon, which we refer to as GW *dephasing*, is sensitive to the

profile of the DM spike and can thus provide valuable insight into the DM distribution around intermediate-mass BHs. Dephasing effects have been extensively studied in the context of collisionless dark matter (CDM) [8, 26–39] and wave-like DM [27, 36–47], including various astrophysical environmental effects [28, 48]. In both cases, a sufficiently dense DM spike can significantly impact a black hole's inspiral.

Self-interacting dark matter (SIDM) models [49–53], where DM particles scatter off each other on timescales comparable to or shorter than halo formation, offer a compelling alternative to conventional collisionless dark matter (CDM). Many studies have shown how certain SIDM models can modify DM structures from dwarf galaxies ($\mathcal{O}(100)$ pc) to galaxy clusters ($\mathcal{O}(10)$ Mpc), addressing various small-scale structure challenges or seeding supermassive BHs (see [54–57] for thorough reviews). The thermalization of SIDM through self-interaction leads to the formation of a lower-density SIDM spike [53], significantly altering the expected density when compared to a CDM spike. This difference directly impacts the GW dephasing, which, if detected, could provide crucial insights into SIDM spikes on much smaller scales ($\mathcal{O}(10^{-8})$ pc), comparable to $\mathcal{O}(10 - 100)$ of the Schwarzschild radius of the intermediate-mass BHs for generating visible LISA signals. While DM interactions have been explored in the context of facilitating supermassive black hole mergers [58], no studies, to our knowledge, have investigated the dephasing signal in the SIDM scenario. This is likely due to the typically low spike density in SIDM, which results in negligible GW dephasing.

In this work, we show that SIDM mediated by force mediators within a specific mass range can sustain a dense enough DM spike, leading to significant GW dephasing. Higher DM velocity dispersion suppresses self-interactions within the spike, resulting in a denser profile than in typical SIDM scenarios. This effect enables LISA to detect GW dephasing and distinguish SIDM interaction strengths based on their effects on core and spike density.

* abanik@cbnu.ac.kr

† Corresponding author: jeonghan.kim@cbu.ac.kr

‡ junseung.pi@cbnu.ac.kr

§ ytsai3@nd.edu

Accurately modeling the interactions between the binary BH and the surrounding DM spike is essential for distinguishing different SIDM models through GW dephasing. In particular, during mergers involving intermediate-mass BHs, the energy injected into the DM spike can be comparable to its binding energy, leading to a feedback effect on the DM halo [33, 59, 60], which can alter the gravitational waveform.

In this *Letter*, we use the N -body simulation code KETJU [61–64] to study the evolution of binary-BH mergers, the surrounding DM spike, and the resulting GW signals. Defining the mass ratio between the lighter and heavier BH as q , we find for inspirals with $q = 10^{-4}$, our dephasing results match estimates based on Chandrasekhar’s formula for dynamical friction [65]. However, for $q = 10^{-2}$, we observe significant deviations due to changes in the DM halo, which reduce the dephasing. By fitting the vacuum waveform to DM-affected signals, we demonstrate that GW detections can probe DM environments by identifying shifts in key waveform parameters. Comparing the shifts with the measurement uncertainties allows us to evaluate LISA’s ability to distinguish DM interaction properties in different signal-to-noise ratios (SNRs).

DM environments around BHs. The DM environment around a given binary-BH is determined by the constituent masses, commonly parameterized by the mass of the heavier BH M_1 and the mass ratio q . For simplicity, we fix $M_1 = 10^4 M_\odot$ and consider cases with $q = 10^{-4}$ and $q = 10^{-2}$. The choice gives the Schwarzschild radius of the binary, $r_s = 2GM_1(1+q) \sim 10^{-9}$ pc. We highlight key features of the DM density profiles here, which we will use later to study the inspiral phase. We provide technical details on obtaining these in App. A.

We assume the heavier BH resides at the galaxy’s center. In the outermost regions, both CDM and SIDM halos follow the Navarro-Frenk-White (NFW) profile, ρ_{NFW} [66, 67]. For CDM, the BH’s influence modifies the NFW profile, forming a dense spike [21, 22]

$$\rho_{\text{spike}}(r) \equiv \rho_{\text{sp}} \left(\frac{r_{\text{sp}}}{r} \right)^{\gamma_{\text{sp}}}, \quad (1)$$

where we take the spike index $\gamma_{\text{sp}} = 7/3$, assuming an adiabatically grown CDM spike [21]. The parameters in the spike profile to be determined are r_{sp} and ρ_{sp} . The spike radius is determined by $r_{\text{sp}} \approx 0.2 r_{2\text{M}}$ [68], where $r_{2\text{M}}$ is the radius up to which the mass enclosed by the NFW profile is twice the mass of the central black hole. Then, continuity between the NFW profile with the spike profile at $r = r_{\text{sp}}$ fixes ρ_{sp} .

For SIDM, we estimate the density profile following [58]. Self-interactions thermalize SIDM particles, forming a core of radius r_c , with the NFW profile for $r \geq r_c$ [53]. The formation of the core depends on the strength of the interaction cross-section satisfying [53, 58]

$$\frac{\langle \sigma v \rangle}{m} \rho_{\text{NFW}}(r_c) t_{\text{age}} \sim 1, \quad (2)$$

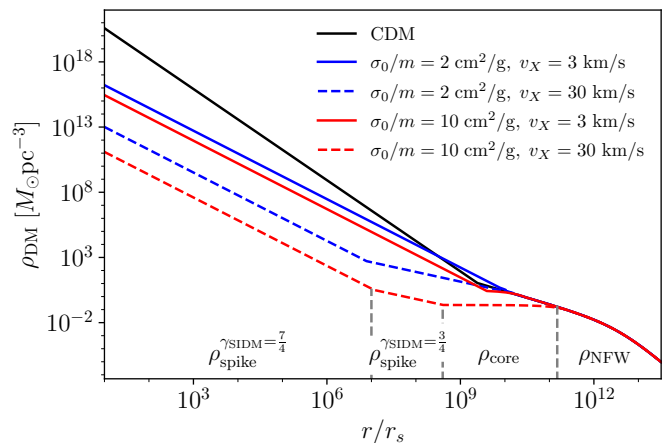


FIG. 1. Examples of SIDM density profiles with different σ_0/m (colored lines) and v_X (solid and dashed lines) around a black hole binary with $M_1 = 10^4 M_\odot$ and $q = 10^{-4}$. We have here $r_s \sim 10^{-9}$ pc. The solid black curve shows the corresponding CDM profile for comparison, while the dashed red curve highlights different regions of the SIDM profile. For numerical study, we use the CDM (solid black), solid blue, and solid red curves, with the binary inspiraling from $r \approx 30 r_s$ and merging at $r \approx 10 r_s$.

i.e., approximately one scattering per DM particle within the core, $r < r_c$, during the age of the core chosen to be $t_{\text{age}} = 0.5$ Gyr [69]. Here, $\langle \sigma v \rangle$ is SIDM’s averaged velocity times cross-section, and m is the DM mass. We model the interaction between DM through the exchange of a particle of mass m_X . Introducing a threshold velocity, $v_X \equiv m_X/m$, the velocity-dependent cross-section behaves as:

$$\sigma(v) = \frac{\sigma_0}{1 + (v/v_X)^4} = \begin{cases} \sigma_0, & v < v_X \equiv \frac{m_X}{m}, \\ \sigma_0 \left(\frac{v_X}{v} \right)^4, & v > v_X. \end{cases} \quad (3)$$

Therefore, for DM velocities smaller than v_X , the interaction is effectively contact-type, and for much larger velocities, it behaves as through the exchange of a massless mediator. To obtain the SIDM core profile ρ_{core} , we solve the Poisson equation $v_0^2 \nabla^2 \ln \rho_{\text{core}}(r) = -4\pi G \rho_{\text{core}}(r)$, where v_0 is the average dispersion velocity in the core and G being Newton’s constant. Since self-interactions simply redistribute particles inside the core, we require the SIDM core mass to match the NFW mass within $r \leq r_c$ [58]. Along with continuity at $r = r_c$ with the NFW profile, these conditions define ρ_{core} . The full details on obtaining the SIDM core are described in App. A.

The SIDM spike follows a similar power-law behavior as (1) as shown in Ref. [70]. However, the exponent varies depending on the interaction type. By identifying $r \leq r_0 = GM_1(1+q)/v_0^2$ as the radius beginning at which the DM motion is influenced primarily by the BHs, the density profile is given by

$$\rho_{\text{spike}}^{\text{SIDM}}(r) = \rho_0 \left(\frac{r_0}{r} \right)^{\gamma_{\text{SIDM}}}, \quad (4)$$

where the spike index is $\gamma_{\text{SIDM}} = 3/4$ ($7/4$) for a contact-type (massless-mediator-type) self-interaction. Ref. [70] also shows that, as a result of solving the governing hydrodynamic equations, there is a corresponding power law for the velocity, $v(r) \sim r^{-1/2}$. This may lead to a change in the interaction type, c.f. (3), which we account for by using the following velocity dispersion [58] [71]

$$v(r) \approx \frac{v_0}{11} \left[7 + 4 \left(\frac{r_0}{r} \right)^{1/2} \right] \quad (5)$$

for the contact-interaction-spike and find the transition radius r_t to the massless-mediator-spike from $v(r_t) = v_X$.

In Fig. 1, we show the CDM profile (black) and examples of SIDM profiles. For a fixed v_X , increasing σ_0/m widens the SIDM core, as observed in the dashed-blue versus dashed-red curves. The wider core leads to suppressed densities in both the spike and core regions. From the core boundary to the halo center, the dashed curves transition from a flat core (contact interaction) to a contact-interaction-spike ($\gamma_{\text{SIDM}} = 3/4$), and finally to a massless-mediator-spike (r_t , $\gamma_{\text{SIDM}} = 7/4$). For heavy mediators (corresponds to $v_X = 30$ km/s), the SIDM spike densities are much lower than in the CDM case. However, with lighter mediators (solid blue and red, $v_X = 3$ km/s), $\sigma(v)$ experiences stronger velocity suppression, allowing a denser $\gamma_{\text{SIDM}} = 7/4$ spike to form near the core boundary, leading to significantly larger spikes.

Below we focus on the $v_X = 3$ km/s scenario, where a ~ 10 pc core and a dense DM spike lead to significant GW dephasing. Observations of dwarf galaxies with radius ~ 10 pc and $\mathcal{O}(1)$ km/s virial velocities [72] suggest that halos with a similar size can exist and may host intermediate-mass BHs. In larger halos with velocity dispersions $\gg 3$ km/s, the self-interactions of the DM become velocity-suppressed, making the DM behave more like CDM.

Binary-BH inspiral and GW dephasing. In this study, we utilize the publicly available KETJU code [61–64] to model the trajectories of binary-BHs and the resulting GW signals. KETJU allows us to track the evolution of binary-BHs from the early stages of their merging process up to the final few orbits before their coalescence. This approach accounts for the dynamical friction exerted by the surrounding DM. Additionally, KETJU incorporates velocity-dependent post-Newtonian (PN) corrections for binary-BHs, providing a more precise representation of their dynamics. In the simulations presented here, PN corrections are applied at 2.5 PN order for the binary motion.

The density profiles obtained in the previous section are used to distribute DM clumps within a non-periodic comoving box, with sizes of $\sim 1 \times 10^8 r_s$ for CDM and $\sim 7 \times 10^4 r_s$ for SIDM, respectively. We choose different box sizes to ensure similar particle numbers in the simulation, as the central density of CDM spike is ~ 4 orders of magnitude larger. The number of DM clumps is set to 32^3 for both CDM and SIDM. For concreteness, we

focus on the self-interaction strength [73] with $\sigma_0 = 2 - 10 \text{ cm}^2/\text{g}$ with $v_X = 3$ and 4 km/s [74]. In App. B, we provide details of our simulations and their implementation. To account for numerical fluctuations, we performed 5 simulations per case using the same setup and similar initial conditions, presenting the averaged results along with uncertainties estimated via $1/\sqrt{N}$ analysis.

The binary merger proceeds through energy losses in the system. In the absence of a DM environment (i.e., in a vacuum), the merger occurs purely through GW emission [75, 76]. Having fixed $M_1 = 10^4 M_\odot$ with a $q = 10^{-4}$ or 10^{-2} , and given that, in our simulation, the binary is defined to merge at $r \approx 10 r_s$, the frequency of the GW at merger is $\sim 10^{-1}$ Hz, which lies in the high sensitivity regime of LISA. We then proceed to set up the inspiral for a merger time of $\tau_{\text{merge}} = 4$ years, corresponding to starting our simulation with the distance between the BHs being $\approx 30 r_s$ ($95 r_s$) for $q = 10^{-4}$ (10^{-2}). This gives frequencies of the emitted GWs in the range of 10^{-3} to 10^{-1} Hz. However, if DM is present around the BHs, it gains energy from their orbital motion, imparting dynamical friction to the binary system and thus accelerating the merger rate [65]. Additionally, the binary’s motion can disrupt DM density profiles, introducing more complex dynamics.

Fig. 2 shows the evolution of CDM and SIDM density profiles around binaries (in different colors) for two mass ratios. For $q = 10^{-4}$, the DM profiles remain largely stable, indicating insufficient orbital energy to disrupt them. At $q = 10^{-2}$, DM density near the initial inspiral radius (right edge of the purple region) drops by up to an order of magnitude, as the lighter BHs clear out DM along their trajectory.

To study the effect of GW dephasing from dynamical friction due to DM, we calculate the total number of orbit cycles accumulated over the merger time τ_f ,

$$N_{\text{cyc}}^{\text{acc}} \equiv \int_0^{\tau_f} f(\tau) d\tau, \quad \tau_f \equiv \tau|_{r=10 r_s}, \quad (6)$$

where f is the instantaneous frequency of the GW signal. As dynamical friction reduces the merger time $\tau_f < \tau_{\text{merge}}$, fewer cycles are accumulated w.r.t. the pure vacuum case, and this is characterized by the *dephasing*

$$\Delta N_{\text{cyc}} = N_{\text{cyc, vac}}^{\text{acc}} - N_{\text{cyc, env}}^{\text{acc}}. \quad (7)$$

Here, the subscript “env” refers to the orbital cycles accumulated for a binary inspiralling within a DM environment.

In order to compare our dephasing results, based on N -body simulations, to static dynamical friction results, we make use of the publicly available code IMRIPy [77, 78], which studies the time-evolution of the binary without incorporating feedback on the DM halo (see App. B for details). For CDM, our simulation gives $\Delta N_{\text{cyc}} = 47302 \pm 21154$ with a BH mass ratio of $q = 10^{-4}$. The static dynamical friction estimate yields $\Delta N_{\text{cyc}} = 21787$, which is within 1.64σ of our simulation result, also being consistent with recent N -body simulations involving

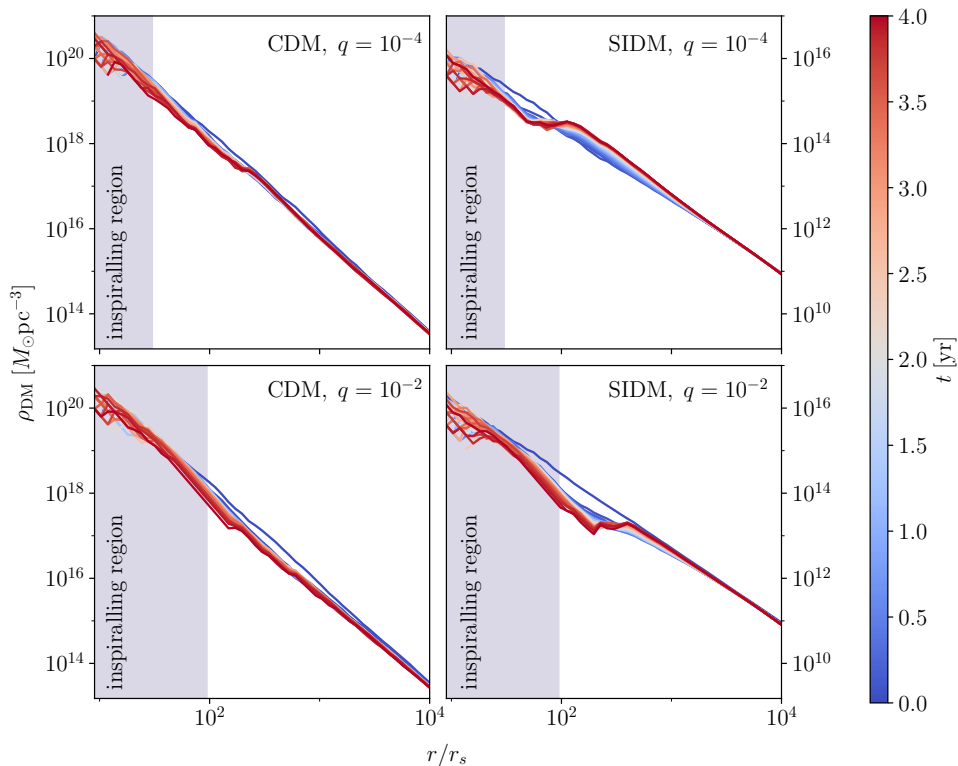


FIG. 2. The evolution of DM density profiles around a BH of mass $10^4 M_\odot$ over the binary merger time of ~ 4 years, for binary mass ratios $q = 10^{-4}$ (top row) and 10^{-2} (lower row). Purple-shaded regions refer to the inspiralling region for the respective binary.

CDM, for e.g. [59]. For a mass ratio of $q = 10^{-2}$, our simulation finds $\Delta N_{\text{cyc}} = 576 \pm 258$, roughly two orders of magnitude smaller than the dynamical friction estimate $\Delta N_{\text{cyc}} = 58636$.

Fig. 3 shows dephasing in SIDM environments for two BH mass ratios, two v_X values, and varying σ_0/m . The data points (blue and red bullets) are from our simulation, and the dashed curves are static dynamical friction model estimates. As in the CDM case, ΔN_{cyc} from the simulation is much smaller than the dynamical friction model estimate for $q = 10^{-2}$. The earlier halt in dephasing for larger q is expected, as the DM density in the inspiral orbit is cleared out sooner. Indeed, for $q = 10^{-2}$, the DM halo is significantly disrupted after about 0.37 years, with ΔN_{cyc} primarily driven by the inspiral motion up to this point. We note that the dephasing, even in this case, is much larger than the ΔN_{cyc} from possible baryonic effects estimated in Refs. [28, 48].

Distinguishing the SIDM environments. To access LISA’s potential in distinguishing GW signals between CDM and different SIDM environments, we use the N_{cyc} template derived assuming no DM environment to fit the early- and late-time evolution of the N_{cyc} spectrum. By comparing the different template parameters obtained from the fit to the expected LISA sensitivity on

these parameters, we can decide if the change of the inspiral evolution due to the DM environment is observable or not.

The N -body simulation provides $N_{\text{cyc}}(f)$ as a function of emitted GW frequency, with lower (higher) frequencies corresponding to the inspiral at earlier (later) times. We fit the spectrum in frequency regions smaller or larger than f_* , which is chosen to minimize the total chi-square of the fit, using the vacuum template [75, 76, 79]:

$$N_{\text{cyc}}^{\text{vac}}(f) = \frac{1}{32\pi^{\frac{8}{3}}} (GM_{\text{ch}})^{-\frac{5}{3}} \left[f^{-\frac{5}{3}} - f_{\text{max}}^{-\frac{5}{3}} \right]. \quad (8)$$

Here, for the lower frequency region $f < f_*$, $f_{\text{max}} = f_*$, whereas for $f > f_*$, f_{max} equals the GW frequency at merger time when $r = 10 r_s$. The chirp mass is defined as $M_{\text{ch}} = M_1 q^{3/5} / (1 + q)^{1/5}$. For $M_1 = 10^4 M_\odot$ and $q = 10^{-4}$ (10^{-2}), we get $M_{\text{ch}} \approx 39.81 M_\odot$ ($629.70 M_\odot$). However, fitting the simulation results for different DM environments using (8) requires corrections δM_{ch} to match the data, and we calculate the chirp mass difference

$$\delta M_{\text{ch}}^i \equiv \delta M_{\text{ch}}^{i, f < f_*} - \delta M_{\text{ch}}^{i, f > f_*} \quad (9)$$

for $i = \text{vacuum, CDM, or SIDM}$ models between the two frequency regions. Without requiring phase measurements from an extremely early time to determine the difference in total N_{cyc} , δM_{ch}^i allows us to distinguish between the early- and late-time evolution of the

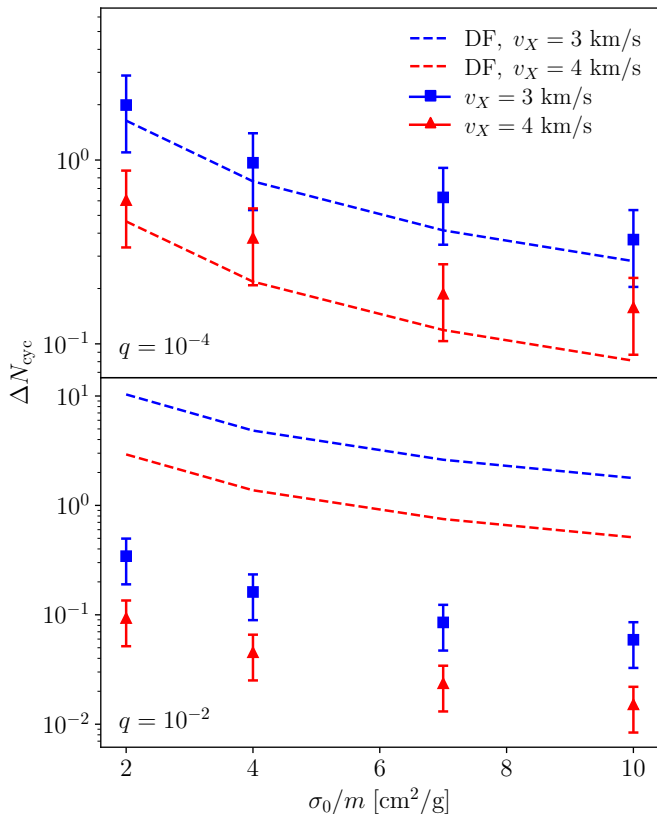


FIG. 3. The dephasing obtained for the SIDM environment from our simulation, for various σ_0/m , $v_X = 3$ km/s (blue squares) and 4 km/s (red triangles), and BH mass ratios $q = 10^{-4}$ (upper panel) and 10^{-2} (lower panel). We show the dephasing obtained assuming no feedback on the DM halo from the secondary BH (blue and red dashed lines). The error bars on the bullets are based on $1/\sqrt{N}$ analysis of the 5 simulations per case we performed.

inspiral across different DM environments. We provide more technical details of the fitting procedure, as well as the results, in App. C.

To access LISA’s ability in distinguishing $N_{\text{cyc}}(f)$ across DM environments, we check if $\delta M_{\text{ch}}^{\text{CDM}} - \delta M_{\text{ch}}^{\text{vac}}$ and $\delta M_{\text{ch}}^{\text{SIDM}} - \delta M_{\text{ch}}^{\text{CDM}}$ can be larger than the expected LISA sensitivity of the M_{ch} measurement. Using **GWFish** [80], a Fisher matrix-based tool to forecast parameter uncertainties in GW signals, we estimate the measurement uncertainty of M_{ch} by LISA. Given the merger time $\tau_{\text{merge}} = 4$ years, we vary the luminosity distance from 20 – 120 Mpc (500 – 3500 Mpc) for $q = 10^{-4}$ (10^{-2}), to forecast observations with SNRs 15, 40, and 100, obtaining the corresponding uncertainties on the chirp masses.

For the phase difference between the CDM and vacuum environments, we find $|\delta M_{\text{ch}}^{\text{CDM}} - \delta M_{\text{ch}}^{\text{vac}}| = (0.512351 \pm 0.22913) M_{\odot}$ for $q = 10^{-4}$ and $(0.140593 \pm 0.062875) M_{\odot}$ for $q = 10^{-2}$. These differences surpass LISA’s sensitivity, even with a modest SNR of 15, capable of detecting $\delta M_{\text{ch}} \approx 2.5 \times 10^{-5} M_{\odot}$. This demonstrates LISA’s ability to effectively distinguish the $N_{\text{cyc}}(f)$ evolutions between

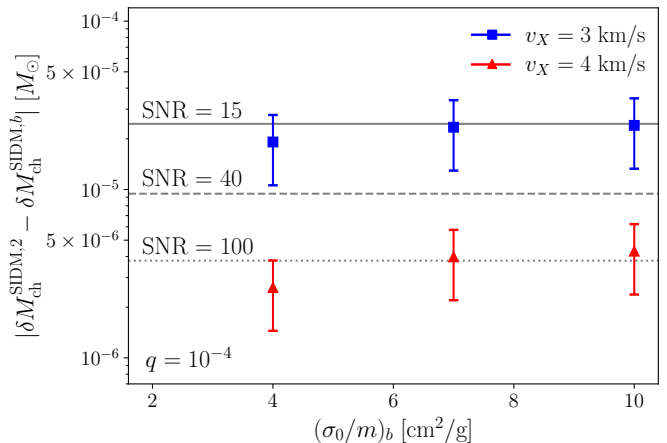


FIG. 4. The shifts in the chirp mass for N_{cyc} measurements for $q = 10^{-4}$ with SIDM environments. We compare the shifts of the profile featuring $\sigma_0/m = 2 \text{ cm}^2/\text{g}$ against others, labeled with the subscript b . Blue squares (red triangles) show the averaged results from the 5 simulations we performed, for $v_X = 3$ (4) km/s, with the error bars based on the $1/\sqrt{N}$ analysis. Gray lines mark the uncertainties on the measurement of the chirp mass by LISA for various SNRs, as calculated using **GWFish**, assuming luminosity distances of 125 (solid), 60 (dashed) and 20 (dotted) Mpc.

CDM and SIDM spikes.

If LISA detects the small $\delta M_{\text{ch}}^{\text{SIDM}}$ predicted by our SIDM model, can it distinguish the δN_{cyc} variations between different SIDM interaction strengths? In Fig. 4, we compare $\delta M_{\text{ch}}^{\text{SIDM}}$ for different values of σ_0/m , using $\sigma_0/m = 2 \text{ cm}^2/\text{g}$ as a reference, with $v_X = 3$ or 4 km/s for $q = 10^{-4}$. Even though the GW dephasing from SIDM is much smaller, LISA can still differentiate between interaction strengths with $\text{SNR} \approx 40$ for $v_X = 3$ km/s and $\text{SNR} \approx 100$ for $v_X = 4$ km/s. However, for $q = 10^{-2}$, the SIDM spike is significantly disrupted, causing dephasing to end earlier, making ΔN_{cyc} differences too small for LISA to resolve (see App. C).

Conclusion. DM surrounding binary BHs affects merger dynamics by inducing dynamical friction, leading to GW dephasing during the inspiral phase. This dephasing depends on the DM spike profile, which can be altered by self-interactions. While SIDM typically forms a core that reduces spike density, we show that velocity-dependent SIDM with a massive mediator can sustain a dense enough spike to produce a detectable dephasing signal at LISA. Using N -body simulations, we analyze GWs from binary-BH inspirals in both CDM and SIDM, tracking dephasing through chirp mass shifts derived from fitting early- and late-time inspiral motion to a vacuum template. Our results indicate that LISA can distinguish DM spikes in CDM and SIDM scenarios and resolve different SIDM interaction strengths. This suggests that intermediate-mass BH inspirals offer a new way to probe SIDM structure on much smaller scales than those typically considered in dwarf galaxies.

ACKNOWLEDGMENTS

We would like to thank Peter H. Johansson for his valuable comments and for providing the publicly available KETJU code. AB, JHK and JP are supported by the Basic Science Research Program through the National Research Foundation of Korea (NRF) funded by the Ministry of Education under grant number [NRF-2021R1C1C1005076], and partly by the Institute of Information & Communications Technology Planning & Evaluation (IITP)-Information Technology Research Center (ITRC) grant [IITP-2025-RS-2024-00437284, 20%]. AB also receives support from the NRF, under grant number [NRF-2020R1I1A3068803]. YT is supported by the NSF Grant PHY-2412701. YT would like to thank the Tom and Carolyn Marquez Chair Fund for its generous support and the Aspen Center for Physics (supported by NSF grant PHY-2210452). YT would also like to thank Munich Institute for Astro-, Particle and BioPhysics (MI-APbP) which is funded by the Deutsche Forschungsgemeinschaft (DFG, German Research Foundation) under Germany's Excellence Strategy – EXC-2094 – 390783311.

Appendix A: Dark matter density profiles

In this appendix, we expound on the DM density profiles used. As mentioned in the main text, the outermost part of the DM halo is described by the NFW profile:

$$\rho_{\text{NFW}}(r) \equiv \frac{\rho_{\text{sc}}}{\left(\frac{r}{r_{\text{sc}}}\right) \left(1 + \frac{r}{r_{\text{sc}}}\right)^2}, \quad (\text{A.1})$$

$$\text{with } \rho_{\text{sc}} \equiv \frac{\rho_{\text{cr}} \Delta}{3} \frac{\mathbf{c}^3}{\ln(1 + \mathbf{c}) - \mathbf{c}/(1 + \mathbf{c})}.$$

Here, $\rho_{\text{cr}} = 2.775 \times 10^{11} h^2 M_{\odot} \text{Mpc}^{-3}$ is the critical density for a spatially flat Universe with $h = 0.674$ being the value of the reduced Hubble constant today, as inferred from the CMB [81]. We have defined the concentration parameter $\mathbf{c} = r_{\text{vir}}/r_{\text{sc}}$ as the ratio between the virial radius to the scaling radius, with r_{vir} being defined as the radius at which the $\rho_{\text{NFW}} = \rho_{\text{cr}} \Delta$. Setting $\Delta = 200$, as is standard, we use the relation between \mathbf{c} and the virial (halo) mass M_{200} described in [82]. These fix the parameters ρ_{sc} and r_{sc} used to determine the NFW profile.

To describe the CDM spike profile, we need to obtain the parameters r_{sp} and ρ_{sp} . We use the conditions

$$4\pi \int_{r_{\text{min}}}^{5r_{\text{sp}}} dr r^2 \rho_{\text{NFW}}(r) = 2M_1(1 + q), \quad (\text{A.2})$$

$$\rho_{\text{spike}}(r_{\text{sp}}) = \rho_{\text{NFW}}(r_{\text{sp}}), \quad (\text{A.3})$$

which gives two equations to solve for two unknown parameters. Here $r_{\text{min}} = 10 r_s$, the separation distance at which the binary is defined to merge (see main text).

For SIDM, we need to first numerically solve the Poisson equation to determine the SIDM core profile, which

we do by going along the lines of Ref. [58]. Assuming spherical symmetry, we have

$$\left(\frac{d^2}{dr^2} + \frac{2}{r} \frac{d}{dr}\right) \ln \rho_{\text{core}}(r) = -\frac{4\pi G}{v_0^2} \rho_{\text{core}}(r), \quad (\text{A.4})$$

subject to the following boundary conditions

$$\rho_{\text{core}}(r_c) = \rho_{\text{NFW}}(r_c) \equiv \rho_c, \quad \rho'_{\text{core}}(0) = 0, \quad (\text{A.5})$$

along with the mass conservation constraint [58]

$$\int_{r_{\text{min}}}^{r_c} dr r^2 \rho_{\text{core}}(r) = \int_{r_{\text{min}}}^{r_c} dr r^2 \rho_{\text{NFW}}(r). \quad (\text{A.6})$$

Note that r_c is implicitly determined by the condition (2), which we re-write in the following parameterization:

$$\frac{\sigma_0 v_0}{m} \left(\frac{v_X}{v_0}\right)^a \rho_{\text{NFW}}(r_c) t_{\text{age}} \sim 1, \quad (\text{A.7})$$

where $a = 0$ refers to contact-type interactions and for $a = 4$, we have massless-mediator type interactions. We first assume $a = 0$ to solve for the core profile.

It is convenient to switch to dimensionless variables $x \equiv r/r_c$ and $y = \ln(\rho_{\text{core}}/\rho_c)$, which transforms (A.5) into

$$y'' + \frac{2}{x} y' = -C e^y, \quad (\text{A.8})$$

where $C = 4\pi G \rho_c r_c^2 / v_0^2$. The boundary conditions and mass conservation constraint now read as

$$y(1) = 0, \quad y'(0) = 0, \quad (\text{A.9})$$

$$\int_{x_{\text{min}}}^1 dx x^2 e^y = \int_{x_{\text{min}}}^1 dx \frac{x(1+k)^2}{(1+kx)^2}, \quad (\text{A.10})$$

where $k = r_c/r_{\text{sc}}$ and $x_{\text{min}} = r_{\text{min}}/r_c$. For a given value of C , this differential equation can be solved to obtain the core profile. One may approach this as a shooting problem, i.e. by guessing $y(0) = y_0$ for a fixed C to match the boundary condition $y(1) = 0$. As is typical with the shooting method, there arises a degeneracy in that there may be more than one value of y_0 that satisfies the boundary conditions for a given value of C . In this case, we check that the mass conservation constraint, for a given $k < 1$, is satisfied with a tolerance of less than 0.1% to accept the correct value of y_0 . Accordingly, one obtains the dispersion velocity in the core, which is compared to v_X . If $v_0 > v_X$, contact-type interactions are valid in the core with a possible transition occurring according to

$$v(r) = \frac{v_0}{11} \left[7 + 4 \left(\frac{r_0}{r}\right)^{1/2}\right]. \quad (\text{A.11})$$

Otherwise, the massless mediator-type interaction is valid throughout the whole profile; accordingly, we switch to $a = 4$, and repeat the above steps to obtain the profile.

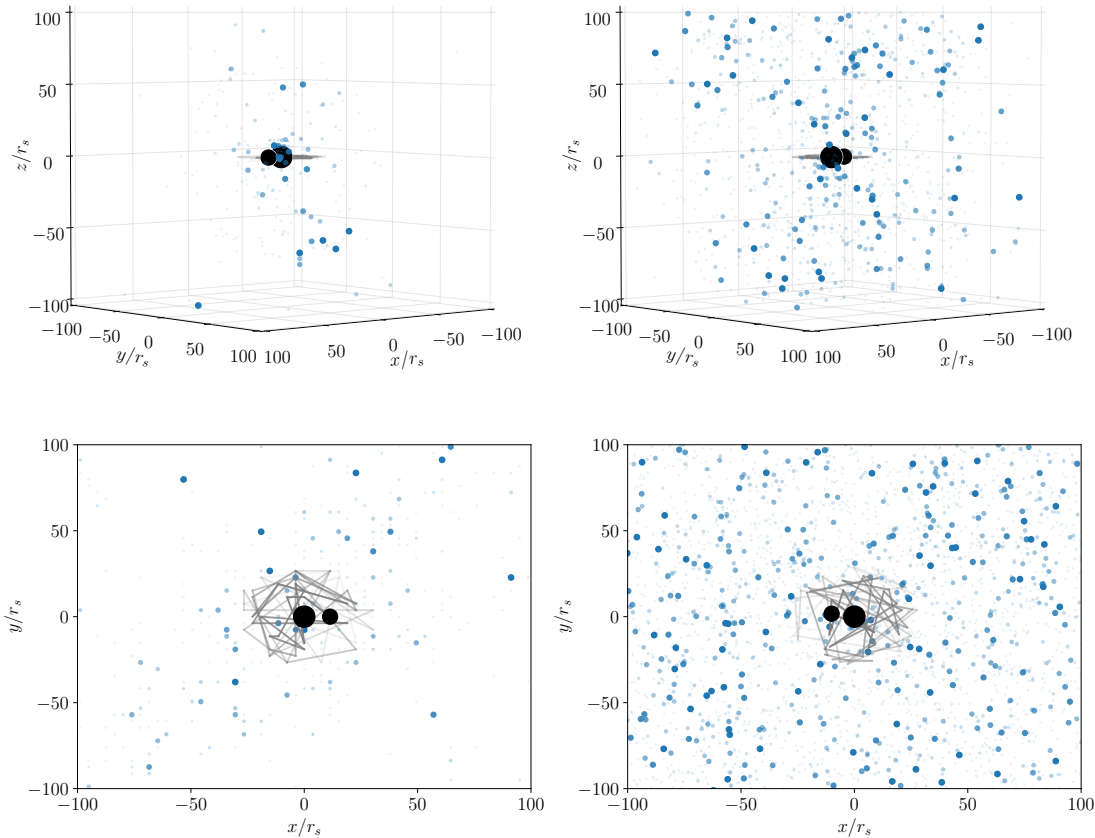


FIG. 5. Snapshots of our N -body simulation in 3D (top row) and the projected 2D plane (bottom row), with the trajectories traced by the smaller BH (smaller black dot) around the central BH (larger black dot) in DM environments (blue dots) shown as gray lines, with opacity indicating increasing time. Note that we maintain the same mass of DM clumps for the particular case, but for illustrative purposes, the increasing size and blue opacity of the DM clumps indicate closer merger times. We show inspirals with $q = 10^{-4}$ in a CDM spike (left column) and an SIDM spike (right column) with $\sigma_0/m = 2 \text{ cm}^2/\text{g}$ and $v_X = 3 \text{ km/s}$. The masses of the DM clumps are different for CDM and SIDM to account for the different density profiles, leading to more DM clumps for SIDM than CDM (see main text for details).

The SIDM core is then superseded by a spike profile. The dispersion velocity determined earlier gives the radius of the transition $r_0 = GM_1(1+q)/v_0^2$, with continuity

$$\rho_{\text{core}}(r_0) = \rho_{\text{spike}}^{\text{SIDM}}(r_0), \quad (\text{A.12})$$

determining the missing parameter ρ_0 for the SIDM spike profile.

Finally, we found it convenient to use the following fitting function to describe the core

$$\rho_{\text{core}}^{\text{fit}}(r) = \frac{\rho_{\text{fit}} r_{\text{fit}}^3}{(r_{\text{fit}} + r)(r_{\text{fit}}^2 + r^2)}, \quad r_0 \leq r \leq r_{\text{fit}}, \quad (\text{A.13})$$

where the parameters r_{fit} and ρ_{fit} are determined by matching to the NFW profile at r_{fit} and to the SIDM spike profile at r_0 .

Appendix B: Simulating binary-BH inspirals with KETJU

We provide here further details on our simulation setup and inclusion of DM self-interactions. Firstly, we use the obtained density profiles to distribute the DM particles. This is done as follows: the mass of DM within a given radius is determined by integrating the density profile

$$M(r) = 4\pi \int_{r_{\text{min}}}^r du u^2 \rho(u). \quad (\text{B.1})$$

Using the relation $M(r) = m_{\text{DM}} N(r)$, where m_{DM} is the mass of a DM clump, we then calculate the number of DM particles at radius r , denoted as $N(r)$. For CDM, we set $m_{\text{DM}} \sim 10^{-3} M_{\odot}$, while for SIDM, we use m_{DM} in the range of 10^{-7} – $10^{-9} M_{\odot}$. A larger value of m_{DM} is chosen for CDM due to the higher density of the CDM

spike profile. These choices ensure that the total number of DM clumps remains around $\sim \mathcal{O}(1000)$ in all cases, allowing for a fair comparison between CDM and SIDM. Simulating the modified KETJU code with an SIDM environment for a merger time of $\tau_{\text{merge}} \sim 4$ years requires approximately 3 days using 1 CPU cores of an Intel(R) Xeon(R) Gold 5416S. In Fig. 5, we show snapshots of our N -body simulation for inspirals in CDM and SIDM environments.

Next, we analyze the contributions of GW emission and dynamical friction to assess their effects on orbital shrinkage within a DM environment. This comparison aims to provide a naïve order-of-magnitude estimate using analytical formulae.

The power emitted in GWs, at 2.5PN order, is given by [75],

$$P_{\text{GW}} = \frac{32G^4 \mu^2 M^3}{5c^5 a^5} \frac{(1 + \frac{73}{24}e^2 + \frac{37}{96}e^4)}{(1 - e^2)^{7/2}}, \quad (\text{B.2})$$

where $M \equiv M_1(1 + q)$ represents the total mass of the binary-BH system, $\mu \equiv qM_1/(1 + q)$ is the reduced mass, a denotes the semi-major axis, and e is the eccentricity.

The form of the dynamical friction acting on the orbiting BH through a DM medium is given by [83]

$$P_{\text{DF}} = \frac{4\pi(GqM_1)^2 \rho_{\text{DM}}}{v_2} I(\mathcal{M}, \Lambda) \quad (\text{B.3})$$

where v_2 is the velocity of the second BH orbiting around the central BH and the function I is defined by

$$I(\mathcal{M}, \Lambda) = \begin{cases} \frac{1}{2} \ln \left(\frac{1+\mathcal{M}}{1-\mathcal{M}} \right) - \mathcal{M}, & \mathcal{M} < 1, \\ \frac{1}{2} \ln (1 - \mathcal{M}^{-2}) + \ln \Lambda, & \mathcal{M} > 1, \end{cases} \quad (\text{B.4})$$

where $\Lambda \equiv ct/r_{\text{min}}$ with t representing the time for which the orbiting BH has traveled. The Mach number $\mathcal{M} \equiv v_2/c_s$ characterizes the velocity of the orbiting BH relative to the sound speed, c_s , in the DM medium.

In the supersonic regime, specifically when $\mathcal{M} \gg 1$, the formula simplifies to the conventional steady-state result, $I = \ln(r_{\text{max}}/r_{\text{min}})$, also known as the the Coulomb logarithm, which incorporates the maximum and minimum impact parameters associated with the orbiting BH. We adopt $\ln \Lambda = -0.5 \ln q$, a commonly used approximation in the literature [33, 84, 85]. Although the exact value of the Coulomb term for SIDM varies depending on the magnitude of c_s (c.f. Ref. [60] for more detailed information), this choice is sufficient for our purposes of making a naïve order-of-magnitude estimate.

Appendix C: Fitting GW waveforms

We provide some details on our procedure to fit various templates to observable waveforms from our simulation data, to obtain the various shifts to compare with the detector uncertainties. As mentioned in the main text,

we focus on N_{cyc} , for which the vacuum template can be calculated at the lowest PN order as:

$$N_{\text{cyc}}^{\text{vac}}(f) = \frac{1}{32\pi^{3/8}} (GM_{\text{ch}})^{-5/3} \left[f^{-5/3} - f_{\text{max}}^{-5/3} \right]. \quad (\text{C.1})$$

We then allow M_{ch} to perturb by δM_{ch} , which will be determined by a least-squares fit to $N_{\text{cyc,env}}$, calculated using our simulation data.

To determine the shifts for environmental fits, we fit two separate regions, based on minimizing the goodness-to-fit metric χ^2 in each region. An example of this is displayed in Fig. 6, whereby we fit the vacuum template to the CDM environment. The shift is then determined by

$$\delta M_{\text{ch}}^i \equiv \delta M_{\text{ch}}^{i,f < f_*} - \delta M_{\text{ch}}^{i,f > f_*}, \quad (\text{C.2})$$

where the superscripts refer to the shifts before and after the frequency window (depicted as a vertical gray line in Fig. 6). The exact values obtained for these shifts are given in Tab. I. Analogous to Fig. 4 of the main text, we compare $\delta M_{\text{ch}}^{\text{SIDM}}$ for different values of σ_0/m , with $\sigma_0/m = 2 \text{ cm}^2/\text{g}$ as a reference, with $v_X = 3$ or 4 km/s for $q = 10^{-2}$, in Fig. 7. In this case, the reduced dephasing, due to the disrupted SIDM spikes, results in all of the shifts of the chirp mass lying below the sensitivity of LISA. Therefore, in such a scenario, LISA will not be able to distinguish SIDM properties, at the chosen SNRs.

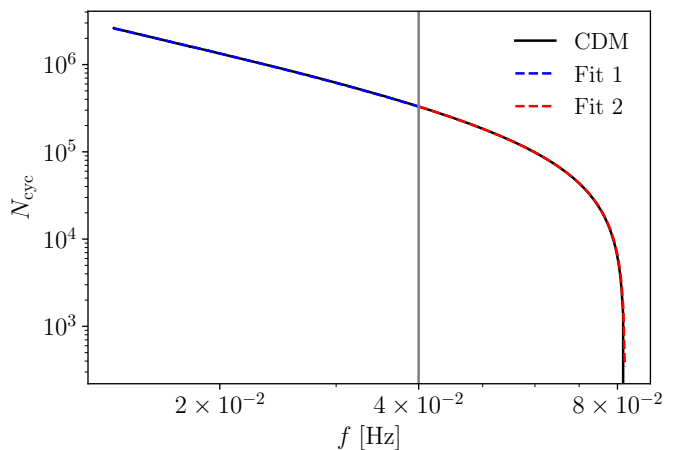


FIG. 6. An example of the fitting procedure employed for CDM data with $q = 10^{-4}$. The grey line separates the two fitting regions, where we calculate the shifts before and after $f_* = 0.04$ Hz.

ENVIRONMENT		$ \delta M_{\text{ch}} [M_{\odot}]$	
		$q = 10^{-4}$	$q = 10^{-2}$
CDM		0.5124	0.1406
SIDM, σ_0/m [cm^2/g]	$v_X = 3 \text{ km/s}$	6.416×10^{-5}	1.887×10^{-3}
	$v_X = 3 \text{ km/s}$	4.494×10^{-5}	1.862×10^{-3}
	$v_X = 3 \text{ km/s}$	4.067×10^{-5}	1.851×10^{-3}
	$v_X = 3 \text{ km/s}$	4.001×10^{-5}	1.847×10^{-3}
$v_X = 4 \text{ km/s}$	$v_X = 4 \text{ km/s}$	4.093×10^{-5}	1.853×10^{-3}
	$v_X = 4 \text{ km/s}$	3.831×10^{-5}	1.845×10^{-3}
	$v_X = 4 \text{ km/s}$	3.695×10^{-5}	1.843×10^{-3}
	$v_X = 4 \text{ km/s}$	3.663×10^{-5}	1.840×10^{-3}

TABLE I. The shifts in the chirp mass when fitting the vacuum template to the environmental results.

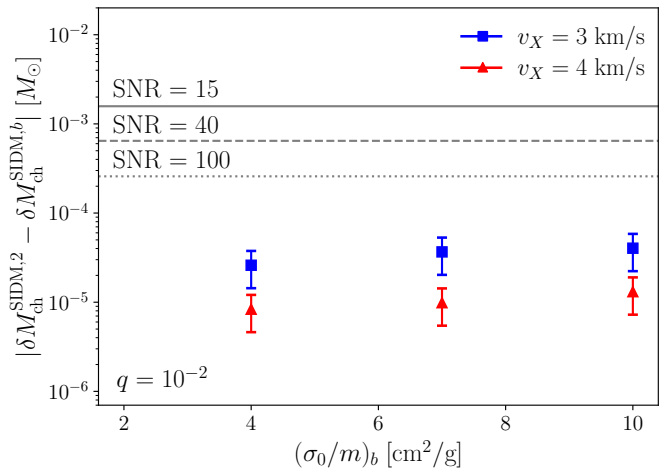


FIG. 7. The shifts in the chirp mass for N_{cyc} measurements for $q = 10^{-2}$ with SIDM environments. We compare the shifts of the profile featuring $\sigma_0/m = 2 \text{ cm}^2/\text{g}$ against others. Blue squares (red triangles) show the averaged results from the 5 simulations we performed, for $v_X = 3$ (4) km/s, with the error bars based on $1/\sqrt{N}$ analysis. Gray lines mark the uncertainties on the measurement of the chirp mass by LISA for various SNRs, as calculated using **GWfish**, assuming luminosity distances of 3200 (solid), 1300 (dashed) and 525 (dotted) Mpc. We see that all the shifts lie below the sensitivity of LISA.

- [1] B. P. Abbott *et al.* (LIGO Scientific, Virgo), GWTC-1: A Gravitational-Wave Transient Catalog of Compact Binary Mergers Observed by LIGO and Virgo during the First and Second Observing Runs, *Phys. Rev. X* **9**, 031040 (2019), [arXiv:1811.12907 \[astro-ph.HE\]](#).
- [2] B. P. Abbott *et al.* (LIGO Scientific, Virgo), GW170817: Observation of Gravitational Waves from a Binary Neutron Star Inspiral, *Phys. Rev. Lett.* **119**, 161101 (2017), [arXiv:1710.05832 \[gr-qc\]](#).
- [3] B. P. Abbott *et al.* (LIGO Scientific, Virgo, Fermi GBM, INTEGRAL, IceCube, AstroSat Cadmium Zinc Telluride Imager Team, IPN, Insight-Hxmt, ANTARES, Swift, AGILE Team, 1M2H Team, Dark Energy Camera GW-EM, DES, DLT40, GRAWITA, Fermi-LAT, ATCA, ASKAP, Las Cumbres Observatory Group, OzGrav, DWF (Deeper Wider Faster Program), AST3, CAAS-TRO, VINROUGE, MASTER, J-GEM, GROWTH, JAGWAR, CaltechNRAO, TTU-NRAO, NuSTAR, Pan-STARRS, MAXI Team, TZAC Consortium, KU, Nordic Optical Telescope, ePESSTO, GROND, Texas Tech University, SALT Group, TOROS, BOOTES, MWA, CALET, IKI-GW Follow-up, H.E.S.S., LOFAR, LWA, HAWC, Pierre Auger, ALMA, Euro VLBI Team, Pi of Sky, Chandra Team at McGill University, DFN, ATLAS Telescopes, High Time Resolution Universe Survey, RIMAS, RATIR, SKA South Africa/MeerKAT), Multi-messenger Observations of a Binary Neutron Star Merger, *Astrophys. J. Lett.* **848**, L12 (2017), [arXiv:1710.05833 \[astro-ph.HE\]](#).
- [4] B. P. Abbott *et al.* (LIGO Scientific, Virgo), Observation of Gravitational Waves from a Binary Black Hole Merger, *Phys. Rev. Lett.* **116**, 061102 (2016), [arXiv:1602.03837 \[gr-qc\]](#).
- [5] R. Abbott *et al.* (KAGRA, VIRGO, LIGO Scientific), Open Data from the Third Observing Run of LIGO, Virgo, KAGRA, and GEO, *Astrophys. J. Suppl.* **267**, 29 (2023), [arXiv:2302.03676 \[gr-qc\]](#).
- [6] M. Baryakhtar *et al.*, Dark Matter In Extreme Astrophysical Environments, in *Snowmass 2021* (2022) [arXiv:2203.07984 \[hep-ph\]](#).
- [7] R. X. Adhikari *et al.*, Report of the Topical Group on Cosmic Probes of Fundamental Physics for for Snowmass 2021, (2022), [arXiv:2209.11726 \[hep-ph\]](#).
- [8] G. Bertone *et al.*, Gravitational wave probes of dark matter: challenges and opportunities, *SciPost Phys. Core* **3**, 007 (2020), [arXiv:1907.10610 \[astro-ph.CO\]](#).
- [9] R. Alves Batista *et al.*, EuCAPT White Paper: Opportunities and Challenges for Theoretical Astroparticle Physics in the Next Decade, (2021), [arXiv:2110.10074 \[astro-ph.HE\]](#).
- [10] A. L. Miller, Gravitational wave probes of particle dark matter: a review, (2025), [arXiv:2503.02607 \[astro-ph.HE\]](#).
- [11] K. G. Arun *et al.* (LISA), New horizons for fundamental physics with LISA, *Living Rev. Rel.* **25**, 4 (2022), [arXiv:2205.01597 \[gr-qc\]](#).
- [12] P. Amaro-Seoane *et al.* (LISA), Laser interferometer space antenna, (2017), [arXiv:1702.00786 \[astro-ph.IM\]](#).
- [13] P. A. Seoane *et al.* (eLISA), The Gravitational Universe, (2013), [arXiv:1305.5720 \[astro-ph.CO\]](#).

- [14] L. Barack and C. Cutler, LISA capture sources: Approximate waveforms, signal-to-noise ratios, and parameter estimation accuracy, *Phys. Rev. D* **69**, 082005 (2004), [arXiv:gr-qc/0310125](#).
- [15] N. Webb, D. Cseh, E. Lenc, O. Godet, D. Barret, S. Corbel, S. Farrell, R. Fender, N. Gehrels, and I. Heywood, Radio Detections During Two State Transitions of the Intermediate Mass Black Hole HLX-1, *Science* **337**, 554 (2012), [arXiv:1311.6918 \[astro-ph.HE\]](#).
- [16] R. R. Islam, J. E. Taylor, and J. Silk, Massive black hole remnants of the first stars in galactic haloes, *Mon. Not. Roy. Astron. Soc.* **340**, 647 (2003), [arXiv:astro-ph/0208189](#).
- [17] G. Bertone, A. R. Zentner, and J. Silk, A new signature of dark matter annihilations: gamma-rays from intermediate-mass black holes, *Phys. Rev. D* **72**, 103517 (2005), [arXiv:astro-ph/0509565](#).
- [18] H.-S. Zhao and J. Silk, Mini-dark halos with intermediate mass black holes, *Phys. Rev. Lett.* **95**, 011301 (2005), [arXiv:astro-ph/0501625](#).
- [19] V. Rashkov and P. Madau, A Population of Relic Intermediate-Mass Black Holes in the Halo of the Milky Way, *Astrophys. J.* **780**, 187 (2014), [arXiv:1303.3929 \[astro-ph.CO\]](#).
- [20] G. D. Quinlan, L. Hernquist, and S. Sigurdsson, Models of Galaxies with Central Black Holes: Adiabatic Growth in Spherical Galaxies, *Astrophys. J.* **440**, 554 (1995), [arXiv:astro-ph/9407005](#).
- [21] P. Gondolo and J. Silk, Dark matter annihilation at the galactic center, *Phys. Rev. Lett.* **83**, 1719 (1999), [arXiv:astro-ph/9906391](#).
- [22] P. Ullio, H. Zhao, and M. Kamionkowski, A Dark matter spike at the galactic center?, *Phys. Rev. D* **64**, 043504 (2001), [arXiv:astro-ph/0101481](#).
- [23] D. Merritt, M. Milosavljević, L. Verde, and R. Jimenez, Dark matter spikes and annihilation radiation from the galactic center, *Phys. Rev. Lett.* **88**, 191301 (2002).
- [24] D. Merritt, Evolution of the dark matter distribution at the galactic center, *Phys. Rev. Lett.* **92**, 201304 (2004).
- [25] G. Bertone and D. Merritt, Time-dependent models for dark matter at the Galactic Center, *Phys. Rev. D* **72**, 103502 (2005), [arXiv:astro-ph/0501555](#).
- [26] K. Eda, Y. Itoh, S. Kuroyanagi, and J. Silk, New probe of dark-matter properties: Gravitational waves from an intermediate-mass black hole embedded in a dark-matter minispikes, *Phys. Rev. Lett.* **110**, 221101 (2013), [arXiv:1301.5971 \[gr-qc\]](#).
- [27] C. F. B. Macedo, P. Pani, V. Cardoso, and L. C. B. Crispino, Into the lair: gravitational-wave signatures of dark matter, *Astrophys. J.* **774**, 48 (2013), [arXiv:1302.2646 \[gr-qc\]](#).
- [28] E. Barausse, V. Cardoso, and P. Pani, Can environmental effects spoil precision gravitational-wave astrophysics?, *Phys. Rev. D* **89**, 104059 (2014), [arXiv:1404.7149 \[gr-qc\]](#).
- [29] K. Eda, Y. Itoh, S. Kuroyanagi, and J. Silk, Gravitational waves as a probe of dark matter minispikes, *Phys. Rev. D* **91**, 044045 (2015), [arXiv:1408.3534 \[gr-qc\]](#).
- [30] X.-J. Yue and W.-B. Han, Gravitational waves with dark matter minispikes: the combined effect, *Phys. Rev. D* **97**, 064003 (2018), [arXiv:1711.09706 \[gr-qc\]](#).
- [31] V. Cardoso and A. Maselli, Constraints on the astrophysical environment of binaries with gravitational-wave observations, *Astron. Astrophys.* **644**, A147 (2020), [arXiv:1909.05870 \[astro-ph.HE\]](#).
- [32] O. A. Hannuksela, K. C. Y. Ng, and T. G. F. Li, Extreme dark matter tests with extreme mass ratio inspirals, *Phys. Rev. D* **102**, 103022 (2020), [arXiv:1906.11845 \[astro-ph.CO\]](#).
- [33] B. J. Kavanagh, D. A. Nichols, G. Bertone, and D. Gaggero, Detecting dark matter around black holes with gravitational waves: Effects of dark-matter dynamics on the gravitational waveform, *Phys. Rev. D* **102**, 083006 (2020), [arXiv:2002.12811 \[gr-qc\]](#).
- [34] A. Coogan, G. Bertone, D. Gaggero, B. J. Kavanagh, and D. A. Nichols, Measuring the dark matter environments of black hole binaries with gravitational waves, *Phys. Rev. D* **105**, 043009 (2022), [arXiv:2108.04154 \[gr-qc\]](#).
- [35] P. S. Cole, G. Bertone, A. Coogan, D. Gaggero, T. Karydas, B. J. Kavanagh, T. F. M. Spieksma, and G. M. Tomaselli, Disks, spikes, and clouds: distinguishing environmental effects on bbh gravitational waveforms, (2022), [arXiv:2211.01362 \[gr-qc\]](#).
- [36] J. Huang, M. C. Johnson, L. Sagunski, M. Sakellariadou, and J. Zhang, Prospects for axion searches with Advanced LIGO through binary mergers, *Phys. Rev. D* **99**, 063013 (2019), [arXiv:1807.02133 \[hep-ph\]](#).
- [37] P. S. Cole, G. Bertone, A. Coogan, D. Gaggero, T. Karydas, B. J. Kavanagh, T. F. M. Spieksma, and G. M. Tomaselli, Distinguishing environmental effects on binary black hole gravitational waveforms, *Nature Astron.* **7**, 943 (2023), [arXiv:2211.01362 \[gr-qc\]](#).
- [38] A. Boudon, P. Brax, P. Valageas, and L. K. Wong, Gravitational waves from binary black holes in a self-interacting scalar dark matter cloud, *Phys. Rev. D* **109**, 043504 (2024), [arXiv:2305.18540 \[astro-ph.CO\]](#).
- [39] J. C. Aurekoetxea, J. Marsden, K. Clough, and P. G. Ferreira, Self-interacting scalar dark matter around binary black holes, *Phys. Rev. D* **110**, 083011 (2024), [arXiv:2409.01937 \[gr-qc\]](#).
- [40] A. Hook and J. Huang, Probing axions with neutron star inspirals and other stellar processes, *JHEP* **06**, 036, [arXiv:1708.08464 \[hep-ph\]](#).
- [41] K. Kadota, J. H. Kim, P. Ko, and X.-Y. Yang, Gravitational wave probes on self-interacting dark matter surrounding an intermediate mass black hole, *Phys. Rev. D* **109**, 015022 (2024), [arXiv:2306.10828 \[hep-ph\]](#).
- [42] D. Croon, A. E. Nelson, C. Sun, D. G. E. Walker, and Z.-Z. Xianyu, Hidden-Sector Spectroscopy with Gravitational Waves from Binary Neutron Stars, *Astrophys. J. Lett.* **858**, L2 (2018), [arXiv:1711.02096 \[hep-ph\]](#).
- [43] H. G. Choi and S. Jung, New probe of dark matter-induced fifth force with neutron star inspirals, *Phys. Rev. D* **99**, 015013 (2019), [arXiv:1810.01421 \[hep-ph\]](#).
- [44] Y. Cao, Y.-Z. Cheng, G.-L. Li, and Y. Tang, Probing vector gravitational atom with eccentric intermediate mass-ratio inspirals, (2024), [arXiv:2411.17247 \[gr-qc\]](#).
- [45] D. Blas, S. Gasparotto, and R. Vicente, Searching for ultralight dark matter through frequency modulation of gravitational waves, *Phys. Rev. D* **111**, 042008 (2025), [arXiv:2410.07330 \[hep-ph\]](#).
- [46] T. Takahashi, H. Omiya, and T. Tanaka, Self-interacting axion clouds around rotating black holes in binary systems, *Phys. Rev. D* **110**, 104038 (2024), [arXiv:2408.08349 \[gr-qc\]](#).
- [47] J. H. Kim and X.-Y. Yang, Gravitational Wave Duet by Resonating Binary Black Holes with Axion-Like Particles, (2024), [arXiv:2407.14604 \[astro-ph.CO\]](#).

- [48] E. Barausse, V. Cardoso, and P. Pani, Environmental Effects for Gravitational-wave Astrophysics, *J. Phys. Conf. Ser.* **610**, 012044 (2015), [arXiv:1404.7140 \[astro-ph.CO\]](#).
- [49] N. Arkani-Hamed, D. P. Finkbeiner, T. R. Slatyer, and N. Weiner, A Theory of Dark Matter, *Phys. Rev. D* **79**, 015014 (2009), [arXiv:0810.0713 \[hep-ph\]](#).
- [50] J. L. Feng, M. Kaplinghat, H. Tu, and H.-B. Yu, Hidden Charged Dark Matter, *JCAP* **07**, 004, [arXiv:0905.3039 \[hep-ph\]](#).
- [51] S. Tulin, H.-B. Yu, and K. M. Zurek, Beyond Collisionless Dark Matter: Particle Physics Dynamics for Dark Matter Halo Structure, *Phys. Rev. D* **87**, 115007 (2013), [arXiv:1302.3898 \[hep-ph\]](#).
- [52] M. Kaplinghat, S. Tulin, and H.-B. Yu, Direct Detection Portals for Self-interacting Dark Matter, *Phys. Rev. D* **89**, 035009 (2014), [arXiv:1310.7945 \[hep-ph\]](#).
- [53] M. Kaplinghat, S. Tulin, and H.-B. Yu, Dark Matter Halos as Particle Colliders: Unified Solution to Small-Scale Structure Puzzles from Dwarfs to Clusters, *Phys. Rev. Lett.* **116**, 041302 (2016), [arXiv:1508.03339 \[astro-ph.CO\]](#).
- [54] A. Kamada, M. Kaplinghat, A. B. Pace, and H.-B. Yu, How the Self-Interacting Dark Matter Model Explains the Diverse Galactic Rotation Curves, *Phys. Rev. Lett.* **119**, 111102 (2017), [arXiv:1611.02716 \[astro-ph.GA\]](#).
- [55] J. S. Bullock and M. Boylan-Kolchin, Small-Scale Challenges to the Λ CDM Paradigm, *Ann. Rev. Astron. Astrophys.* **55**, 343 (2017), [arXiv:1707.04256 \[astro-ph.CO\]](#).
- [56] S. Tulin and H.-B. Yu, Dark Matter Self-interactions and Small Scale Structure, *Phys. Rept.* **730**, 1 (2018), [arXiv:1705.02358 \[hep-ph\]](#).
- [57] W.-X. Feng, H.-B. Yu, and Y.-M. Zhong, Seeding Supermassive Black Holes with Self-interacting Dark Matter: A Unified Scenario with Baryons, *Astrophys. J. Lett.* **914**, L26 (2021), [arXiv:2010.15132 \[astro-ph.CO\]](#).
- [58] G. Alonso-Álvarez, J. M. Cline, and C. Dewar, Self-Interacting Dark Matter Solves the Final Parsec Problem of Supermassive Black Hole Mergers, *Phys. Rev. Lett.* **133**, 021401 (2024), [arXiv:2401.14450 \[astro-ph.CO\]](#).
- [59] D. Mukherjee, A. M. Holgado, G. Ogiya, and H. Trac, Examining the effects of dark matter spikes on eccentric intermediate-mass ratio inspirals using N-body simulations, *Mon. Not. Roy. Astron. Soc.* **533**, 2335 (2024), [arXiv:2312.02275 \[astro-ph.CO\]](#).
- [60] M. S. Fischer and L. Sagunski, Dynamical friction from self-interacting dark matter [10.1051/0004-6361/202451304](#) (2024), [arXiv:2405.19392 \[astro-ph.CO\]](#).
- [61] A. Rantala, P. Pihajoki, P. H. Johansson, T. Naab, N. Lahén, and T. Sawala, Post-Newtonian dynamical modeling of supermassive black holes in galactic-scale simulations, *Astrophys. J.* **840**, 53 (2017), [arXiv:1611.07028 \[astro-ph.GA\]](#).
- [62] M. Mannerkoski, P. H. Johansson, P. Pihajoki, A. Rantala, and T. Naab, Gravitational Waves from the Inspiral of Supermassive Black Holes in Galactic-scale Simulations [10.3847/1538-4357/ab52f9](#) (2019), [arXiv:1909.01373 \[astro-ph.GA\]](#).
- [63] M. Mannerkoski, P. H. Johansson, A. Rantala, T. Naab, S. Liao, and A. Rawlings, Signatures of the Many Supermassive Black Hole Mergers in a Cosmologically Forming Massive Early-type Galaxy, *Astrophys. J.* **929**, 167 (2022), [arXiv:2112.03576 \[astro-ph.GA\]](#).
- [64] M. Mannerkoski, A. Rawlings, P. H. Johansson, T. Naab, A. Rantala, V. Springel, D. Irodotou, and S. Liao, Jet-resolving small-scale supermassive black hole dynamics in gadget-4, *Monthly Notices of the Royal Astronomical Society* **524**, 4062 (2023).
- [65] S. Chandrasekhar, Dynamical Friction. I. General Considerations: the Coefficient of Dynamical Friction, *Astrophys. J.* **97**, 255 (1943).
- [66] J. F. Navarro, C. S. Frenk, and S. D. M. White, The Structure of cold dark matter halos, *Astrophys. J.* **462**, 563 (1996), [arXiv:astro-ph/9508025](#).
- [67] A. V. Maccio', A. A. Dutton, and F. C. v. d. Bosch, Concentration, Spin and Shape of Dark Matter Haloes as a Function of the Cosmological Model: WMAP1, WMAP3 and WMAP5 results, *Mon. Not. Roy. Astron. Soc.* **391**, 1940 (2008), [arXiv:0805.1926 \[astro-ph\]](#).
- [68] D. Merritt, Evolution of the dark matter distribution at the galactic center, *Phys. Rev. Lett.* **92**, 201304 (2004), [arXiv:astro-ph/0311594](#).
- [69] The effect of different core ages has been studied in the context of supermassive BHs in Ref. [58], considering $t_{\text{age}} \sim 0.1 - 1$ Gyr. Increasing t_{age} leads to a wider core (with fixed σ_0/m and v_X); for e.g. increasing t_{age} from 0.5 to 1 Gyr for $(\sigma_0/m, v_X) = (10 \text{ cm}^2/\text{g}, 30 \text{ km/s})$ increases r_c from 320 pc to 740 pc, which can be compensated by increasing σ_0/m to $20 \text{ cm}^2/\text{g}$. All our results can therefore be scaled for larger or smaller t_{age} .
- [70] S. L. Shapiro and V. Paschalidis, Self-interacting dark matter cusps around massive black holes, *Phys. Rev. D* **89**, 023506 (2014), [arXiv:1402.0005 \[astro-ph.CO\]](#).
- [71] We follow this analytic estimate instead of the one in Ref. [70], due to requirement of continuity of the velocities between the core and spike at r_0 .
- [72] A. B. Pace and L. E. Strigari, Scaling Relations for Dark Matter Annihilation and Decay Profiles in Dwarf Spheroidal Galaxies, *Mon. Not. Roy. Astron. Soc.* **482**, 3480 (2019), [arXiv:1802.06811 \[astro-ph.GA\]](#).
- [73] Although our modified code includes the effect of self-interactions, these are inefficient during the observation time of 4 years, c.f. (2). Therefore, σ_0/m essentially is used to determine the SIDM spike density.
- [74] The narrow range of values is chosen to get an observable dephasing, as demonstrated later.
- [75] P. C. Peters, Gravitational Radiation and the Motion of Two Point Masses, *Phys. Rev.* **136**, B1224 (1964).
- [76] M. Maggiore, *Gravitational Waves. Vol. 1: Theory and Experiments* (Oxford University Press, 2007).
- [77] N. Becker, L. Sagunski, L. Prinz, and S. Rastgoo, Circularization versus eccentricification in intermediate mass ratio inspirals inside dark matter spikes, *Phys. Rev. D* **105**, 063029 (2022), [arXiv:2112.09586 \[gr-qc\]](#).
- [78] N. Becker and L. Sagunski, Comparing accretion disks and dark matter spikes in intermediate mass ratio inspirals, *Phys. Rev. D* **107**, 083003 (2023), [arXiv:2211.05145 \[gr-qc\]](#).
- [79] B. Moore, M. Favata, K. G. Arun, and C. K. Mishra, Gravitational-wave phasing for low-eccentricity inspiralling compact binaries to 3PN order, *Phys. Rev. D* **93**, 124061 (2016), [arXiv:1605.00304 \[gr-qc\]](#).
- [80] U. Dupletsa, J. Harms, B. Banerjee, M. Branchesi, B. Goncharov, A. Maselli, A. C. S. Oliveira, S. Ronchini, and J. Tissino, gwfish: A simulation software to evaluate parameter-estimation capabilities of gravitational-wave detector networks, *Astron. Comput.* **42**, 100671 (2023), [arXiv:2205.02499 \[gr-qc\]](#).

- [81] N. Aghanim *et al.* (Planck), Planck 2018 results. VI. Cosmological parameters, *Astron. Astrophys.* **641**, A6 (2020), [Erratum: *Astron. Astrophys.* 652, C4 (2021)], [arXiv:1807.06209](#) [[astro-ph.CO](#)].
- [82] C. A. Correa, J. S. B. Wyithe, J. Schaye, and A. R. Duffy, The accretion history of dark matter haloes – III. A physical model for the concentration–mass relation, *Mon. Not. Roy. Astron. Soc.* **452**, 1217 (2015), [arXiv:1502.00391](#) [[astro-ph.CO](#)].
- [83] E. C. Ostriker, Dynamical friction in a gaseous medium, *Astrophys. J.* **513**, 252 (1999), [arXiv:astro-ph/9810324](#).
- [84] J. Binney and S. Tremaine, *Galactic Dynamics: Second Edition* (2008).
- [85] H. Mo, F. C. van den Bosch, and S. White, *Galaxy Formation and Evolution* (2010).